ADVANCED OPTICAL MATERIALS
www.advopticalmat.de

High Contrast Ultrathin Light-Field Camera Using Inverted Microlens Arrays with Metal–Insulator–Metal Optical Absorber

*Sang-In Bae, Kisoo Kim, Kyung-Won Jang, Hyun-Kyung Kim, and Ki-Hun Jeong**

Light-field imaging has attracted much attention in constructing 3D objects with a simple configuration and capturing all the spatial and directional data in a single photographic exposure. Here, an ultrathin light-field camera (ULFC) for high contrast and high-resolution light-field imaging using a metal–insulator–metal optical absorber based inverted microlens arrays (MIM-iMLA) is reported. A metal–insulator–metal based optical absorber (MIM-OA) between microlenses exhibits high light absorption in the full visible region, thereby highly blocking microlens crosstalk. The MIM-iMLA double the image contrast and improve MTF50 by up to 32%, compared to conventional light-field image. In addition, the MIM-iMLA substantially reduces an image plane distance and brings the objective lens position closer to the MLA. The ULFC exhibits a short total track length of 5.1 mm, demonstrating high contrast light-field image acquisition and high accuracy 3D depth map estimation after light-field rendering. This ultrathin and high contrast light-field camera can provide a new platform for miniaturized 3D cameras in biomedical applications, biometrics, automated inspection, or mobile camera applications.

3D imaging serves as an intriguing technique, expressing intuitive real-world so that humans can better perceive them physically and psychophysically. Recently, 3D imaging techniques are actively utilized for biomedical applications,[1] biometrics,[2] automated optical inspection, military unmanned aerial systems,[3] and mobile cameras[4] to provide accurate 3D objects information. The 3D camera systems are mainly based on stereoscopic vision,[5,6] structured light,[7,8] time-of-flight,[9] or light-field imaging.[10,11] In particular, the light-field camera (LFC) has attracted much attention with a simple configuration without external light sources or additional cameras. The LFC often comprises a single objective lens, microlens arrays (MLA), and a CMOS image sensor. Such a simple configuration samples all the spatial and directional 4D data without focusing on a specific object under a single exposure. The captured data are reconstructed for depth refocusing, sub-aperture imaging, and 3D depth map.[12,13] For decades, light-field rendering techniques have been actively studied in computer vision applications that employ machine learning and neural networks.[14,15] In chorus, LFCs have been focused on improving the imaging qualities by employing new features to MLA such as metalens arrays,[16–18] liquid-crystal based MLA,[19] and multifocal MLA.[20] However, the camera miniaturization, the cost-effectiveness, and the image contrast enhancement are still in need for practical applications. In conventional LFCs, an objective lens focuses on the MLA whose focal length is placed at the image sensor,[10] or the image plane of the objective lens is formed in front of the MLA.[21] Consequently, this unique configuration increases the total track length of the camera, making LFC much thicker than conventional 2D cameras. Besides, conventional MLA often deliver low contrast imaging due to the optical crosstalk caused by the incident light leakage between adjacent microlenses.[22] Crosstalk-free MLA recently employs stacked diaphragm arrays or black silicon structures between microlenses to achieve high contrast imaging. They still have some technical limitations for both short total track length[23,24] and broadband light blocking,[25] respectively. Recently, perfect optical absorbers such as metal–insulator–metal plasmonic structures or nanofilms have been often applied for optical filter, photovoltaic, or solar energy applications, however, not yet for imaging applications.[26–28]

Here we report an ultrathin LFC (ULFC) for high contrast and high-resolution light-field imaging using inverted MLA with a lossy metal–insulator–metal optical absorber (MIM-OA). The ULFC consists of a compact objective lens, metal–insulator–metal aperture microlens arrays (MIM-iMLA), and CMOS image sensor (**Figure 1**a). The MIM-iMLA with a short microlens focal length (f_{MLA}) is inversely integrated into the image sensor to reduce an MLA to image plane distance (B) (Figure 1b). The MIM-OA contains a thin chromium (Cr)-silicon dioxide (SiO_2)-thick Cr. An incident electric field

S.-I. Bae, K. Kim, K.-W. Jang, H.-K. Kim, Prof. K.-H. Jeong
Department of Bio and Brain Engineering
KAIST Institute of Health Science and Technology (KIHST)
Korea Advanced Institute of Science and Technology (KAIST)
291 Daehak-ro, Yuseong-gu, Daejeon 34141, Republic of Korea
E-mail: kjeong@kaist.ac.kr

The ORCID identification number(s) for the author(s) of this article can be found under https://doi.org/10.1002/adom.202001657.

DOI: 10.1002/adom.202001657

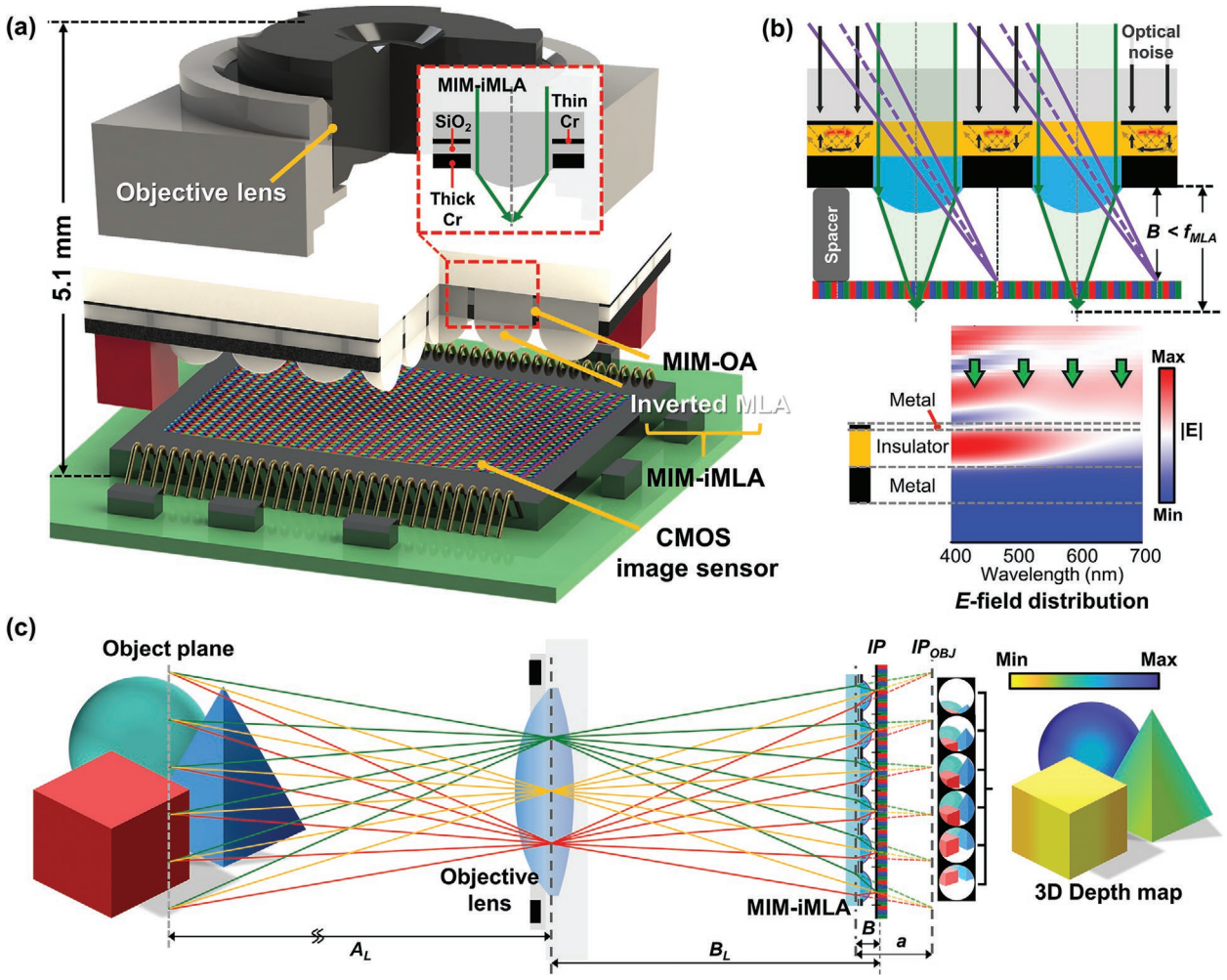

Figure 1. Schematic illustrations and ray diagram of metal–insulator–metal based ULFC. a) The ULFC comprises vertical integration of a compact objective lens, MIM-iMLA, and CMOS image sensor. b) Image acquisition and light absorption of MIM-iMLA. A metal–insulator–metal (Cr–SiO_2–Cr) based optical absorber highly absorbs the visible region light and blocks microlens crosstalk (inset *E*-field distribution). c) Ray diagram of ULFC. An objective lens image lies behind the image sensor (IP_{OBJ}), further reduce total track length. Each microlens generates repeated and upright images with different viewpoints ($f_{MLA} > B$). Raw microimages are reconstructed with high accuracy 3D depth estimation after light-field rendering.

(*E*-field) is highly absorbed through the MIM-OA, compared to the *E*-field distribution passing through the thin Cr film (see Figure S1, Supporting Information, based on the finite difference time domain (FDTD) method). The ULFC is vertically integrated in the order of an objective lens, MIM-iMLA, and a single image sensor based on the Galilean imaging scheme, and repetitive micro-images in an upright form as shown in Figure 1c. The image plane of objective lens lies behind the image sensor (IP_{OBJ}) allowing the objective lens placed closer to the MLA, which substantially reduces the total track length. The f_{MLA} is selected to be longer than the B in the imaging scheme to accurately image on the image sensor (Figure 1b,c). The raw microimages from ULFC are then reconstructed with high accuracy 3D depth estimation after light-field rendering.

The ULFC involves the conventional large-area microfabrication of MIM-iMLA and the compact packaging of an objective lens, MLA, and a single CMOS image sensor (**Figure 2**a). First, a thin DNR photoresist (DNR L300-D1, Dong-jin Semichem, Co., Ltd, Korea) was photo-lithographically defined with a negative shape of Cr microapertures on a 4-inch borosilicate glass wafer. A 5 nm thick Cr layer was then evaporated by using electron beam and lifted off with DNR stripper (DPS-7300, Dong-jin Semichem. Co., Ltd, Korea). A 95 nm thick silicon dioxide was deposited on the wafer by using plasma-enhanced chemical vapor deposition. A 100 nm thick Cr layer was sequentially lifted off on the SiO_2 layer by using the DNR photoresist. The MLA was finally formed on the MIM-OA by using photolithographic definition of DNR photoresist, hydrophobic coating of fluorocarbon, and thermal reflow. Note that the hydrophobic coating effectively prevents the lateral expansion of microlenses on a metal surface during thermal heating. The MIM-iMLA were diced into 5.6 mm × 5.6 mm pieces. Four spacer films of 100 µm in thickness were precisely attached to the edge of CMOS image sensor (Sony IMX 219) and permanently bonded to the MIM-iMLA by using an UV curable adhesive and a flip-chip bonder. An objective lens (f_{OBJ} = 3.04 mm, F/2.0), mechanically separated from Raspberry Pi V2 camera, was permanently mounted on the center of the MIM-iMLA.

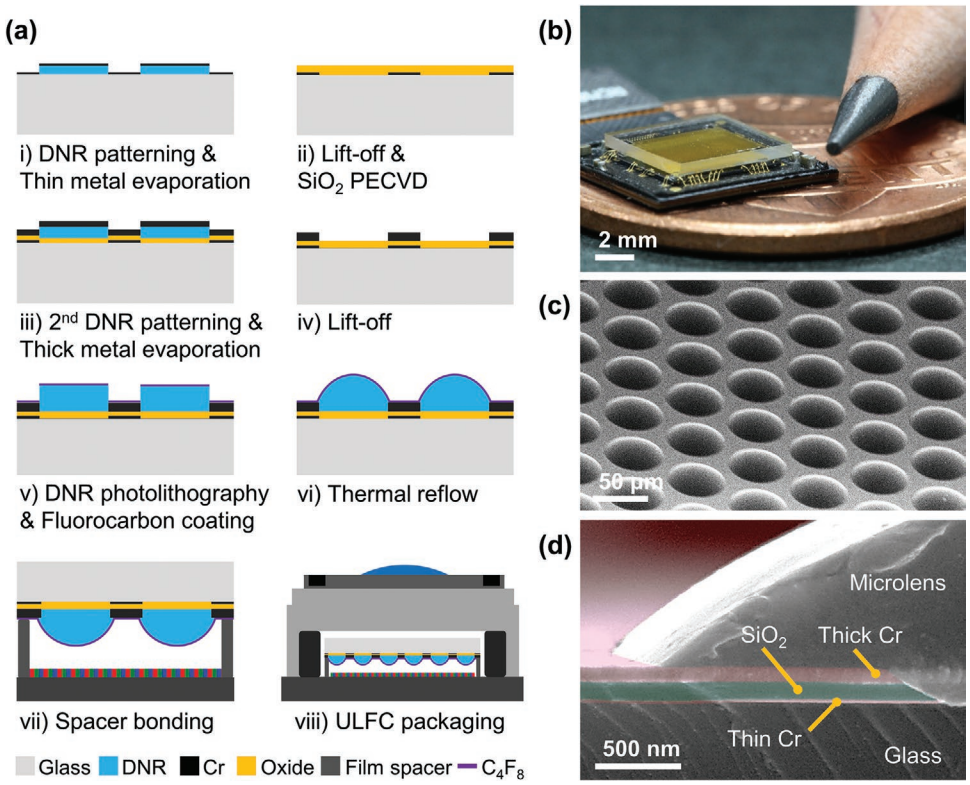

Figure 2. Microfabrication of MIM-iMLA and captured images of MIM-iMLA integrated on CMOS image sensor. a) The monolithic microfabrication of MIM-iMLA includes repetition of Cr lift-off and SiO_2 deposition, photolithography of DNR photoresist, and thermal reflow. Inverted MIM-iMLA are vertically integrated on an image sensor by using a flip-chip bonder and permanently bonded with an objective lens by using a UV curable adhesive. b) A captured photograph of a flip-chip bonded MIM-iMLA and the image sensor. The scanning electron microscopic images of c) perspective and d) cross-sectional MIM-iMLA.

Figure 2b shows a captured photograph of an fully integrated MIM-iMLA on a single image sensor. The scanning electron microscopy images clearly show that the Cr microapertures and microlenses of MIM-iMLA are well aligned with a small overlap area to block MLA cross-talk due to the photolithographic misalignment. (Figure 2c,d).

High contrast imaging via MIM-iMLA results in both micro-images and light-field images. **Figure 3**a compares the optical sections through the MLA without MIM-OA and the MIM-iMLA with 50 μm in diameter and 10 μm in gap, obtained by using a confocal laser scanning microscopy with 533 nm in wavelength. The corresponding normalized intensity along line BB′ on MIM-iMLA shows clear beam focusing and light blocking, compared to that of line AA′ on MLA. The microscopic reflectance images show that the MIM-iMLA (left, Figure 3b) shows low reflectance due to high absorption of visible light whereas the metal-iMLA with a 200 nm thick Cr film (right, Figure 3b) reflect all incident light. The high reflectance of metallic film may cause internal light reflection inside the lens or camera, which degrades the image performance of entire camera (Figures S2 and S3, Supporting Information). All the optimal thicknesses of each MIM-OA using the FDTD method were calculated to have the maximum absorbance in the whole visible region (Figure S4, Supporting Information). As a result, the MIM-iMLA contains 5 nm thick Cr layer, 95 nm thick SiO_2, and 100 nm thick Cr layer. The absorption spectra of 5 nm thick Cr, 100 nm thick Cr, and MIM-OA were also measured for 450–650 nm in wavelength and the measured absorbance at 550 nm in wavelength were 0.05, 0.36, and 0.86, respectively (Figure 3c). A thin chromium film can serve as either absorptive or reflective layer because of its optically lossy nature and less dispersive properties.[27] SiO_2 exhibits high transparency with non-dispersive optical properties in the visible region and thus an incident *E*-field is highly confined by top and bottom Cr layers and trapped in SiO_2. Assuming that a 100 nm thick Cr layer serves as a perfect mirror, an incident *E*-field is partially reflected (γ), transmitted (κ), or absorbed (α) in the MIM-OA. The absorptivity A for unit incidence can be expressed as $A = \alpha^2\kappa^2/[\{(1-\alpha^2)(1-\kappa^2)\}^{0.5} - 1]^2$ at resonance. The MIM-OA causes the destructive interference between incident and reflected *E*-fields, allowing a perfect absorption state ($A = 1$) under the critical coupling condition of $\kappa = \alpha$.[29] The arrayed images captured from the MIM-iMLA show that the black and white lines for a focus test chart target are more clearly separated than those from conventional MLA (Figure 3d). The Michelson contrast, that is, $C = (I_{max} - I_{min})/(I_{max} + I_{min})$, was also calculated from the intensity profiles along AA′ and BB′ lines in Figure 3e, which indicate that MIM-iMLA doubles the image contrast. The light-field image from the ULFC shows a significant improvement in image contrast, compared to that from the LFC without the MIM-OA (Figure 3f). The modulation transfer function (MTF) curves also quantitatively compare

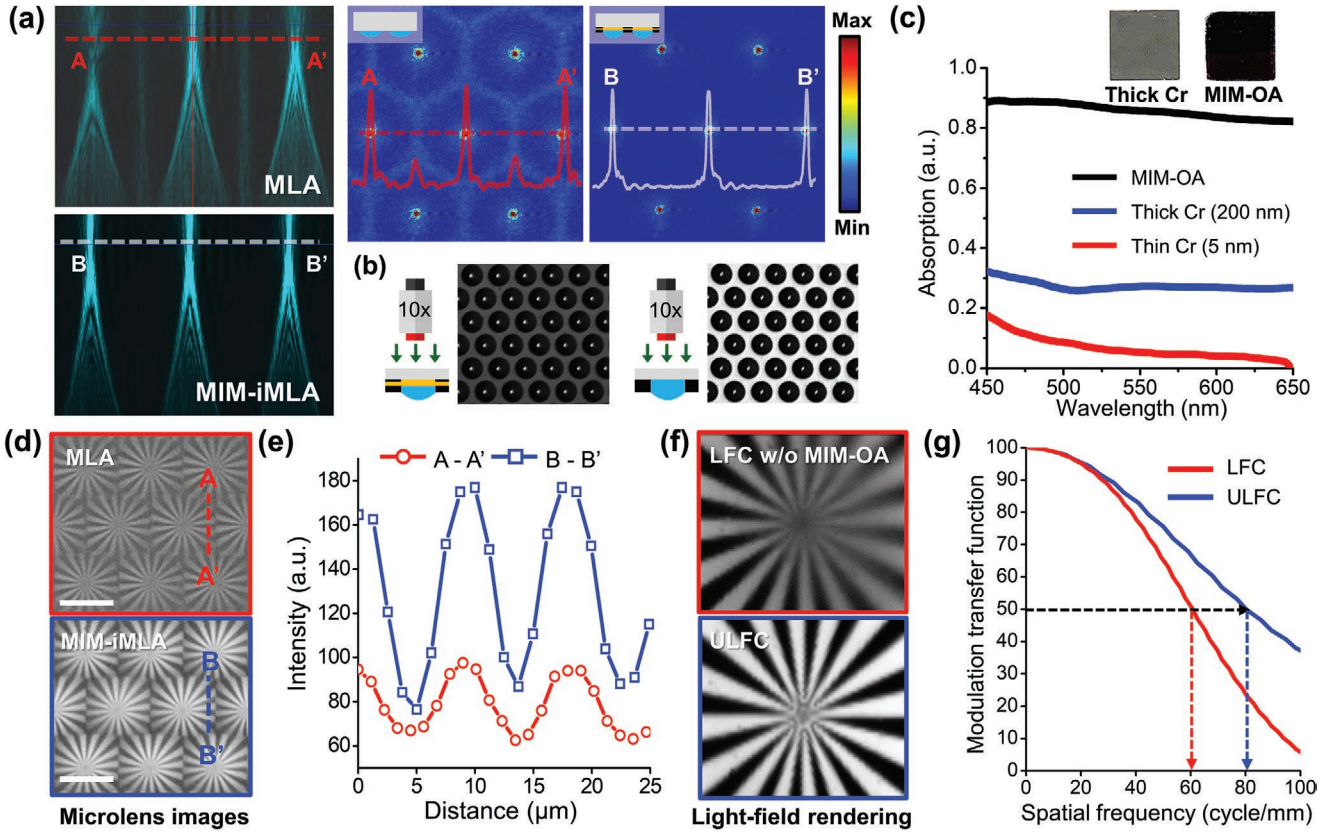

Figure 3. High-contrast light-field imaging through MIM-iMLA. a) Cross-sectional beam profiles and pseudo color intensity maps of MLA and MIM-iMLA, obtained by a confocal laser scanning microscope with 533 nm in wavelength. b) The microscopic images of MIM-iMLA (left) and thick metal-iMLA (right) arrangement. The MIM-iMLA efficiently absorbs the incident light whereas a 200 nm thick Cr film on the metal-iMLA reflects all the incident light. c) Measured light absorption of MIM-OA, a 200 nm thick Cr film, and a 5 nm thick Cr film in the wavelength range of 450–600 nm. The MIM-OA on a glass substrate appears to be a blackbody, while the 200 nm thick Cr film reflects the incident light and looks brighter than the MIM-OA. d) Microimages captured from MLA (top) and MIM-iMLA (bottom) with a diameter of 50 μm and a gap of 10 μm. e) The corresponding intensity profiles along lines AA′ and BB′, respectively. The MIM-iMLA doubles the image contrast. f) Light-field image comparison with LFC without MIM-OA (top) and MIM-iMLA (bottom). g) MTF curves comparison of light-field images through MLA and MIM-iMLA. The MTF50 of ULFC indicates that the ULFC improves image sharpness by 32%.

the image sharpness of light-field images from both the ULFC and the LFC. In particular, the MTF50, which represents the image sharpness, is 80.4 and 60.2 cycles per mm for the ULFC and the LFC, respectively, showing that the MTF50 is improved by 32% (Figure 3g). As a result, the MIM-iMLA significantly increase the image contrast for light-field imaging but also improve the image sharpness.

The ULFC has been fully packaged by using an objective lens, MIM-iMLA, and a single CMOS image sensor to have the minimum total track length. The diameter of MLA (D_{MLA}) was set to 50 μm to achieve high spatial resolution light-field imaging by considering the sizes of an image sensor and the gap spacer distance (B) of 100 μm (Figure S5, Supporting Information). The f-number of MLA (F/2.0) matches that of an objective lens to cover the entire area of an image sensor. In conventional LFCs, f_{OBJ} exists between an objective lens and MLA, so the camera thickness is often increased, and the distance needs to be sufficiently large. Depending on an object position, the objective lens forms an image at a distance a prior to the image sensor (real object $a > 0$ for the Keplerian imaging scheme) or behind the image sensor (virtual object $a < 0$ for the Galilean imaging scheme). In contrast, the ULFC utilizes the Galilean imaging scheme regardless of an object distance and thus significantly decreases total track length by reducing the distance between an objective lens and the MLA. The objective lens forms a virtual object at a distance a from the MLA since f_{OBJ} is behind the image sensor. The corresponding image-side depth-of-field (DOF) range of the objective lens are denoted by a^+ and a^- planes of negative sign. The MLA project a virtual object and thus an object-side DOF of MLA and the image-side DOF of the objective lens are the same as a^+ and a^- planes. Both the planes determine the object-side DOF range of the objective lens, A_L^+ and A_L^-, at a given f_{OBJ} (Detailed calculations on Figure S6, Supporting Information). The DOF satisfying a target object distance was calculated according to each microlens with different f_{MLA}, whose distance is set between 50 and 250 mm considering an inter-pupillary distance for face recognition applications (**Figure 4**a).[30] The tolerable f_{MLA} ranges in 120 μm or less, where the object side DOF range (from A_L^- to A_L^+) covers the target distance, marked as two dotted lines. A virtual depth (v), that is, a ratio of a to B ($v = |a|/B$), is inversely proportional to the spatial resolution so that f_{MLA} is set

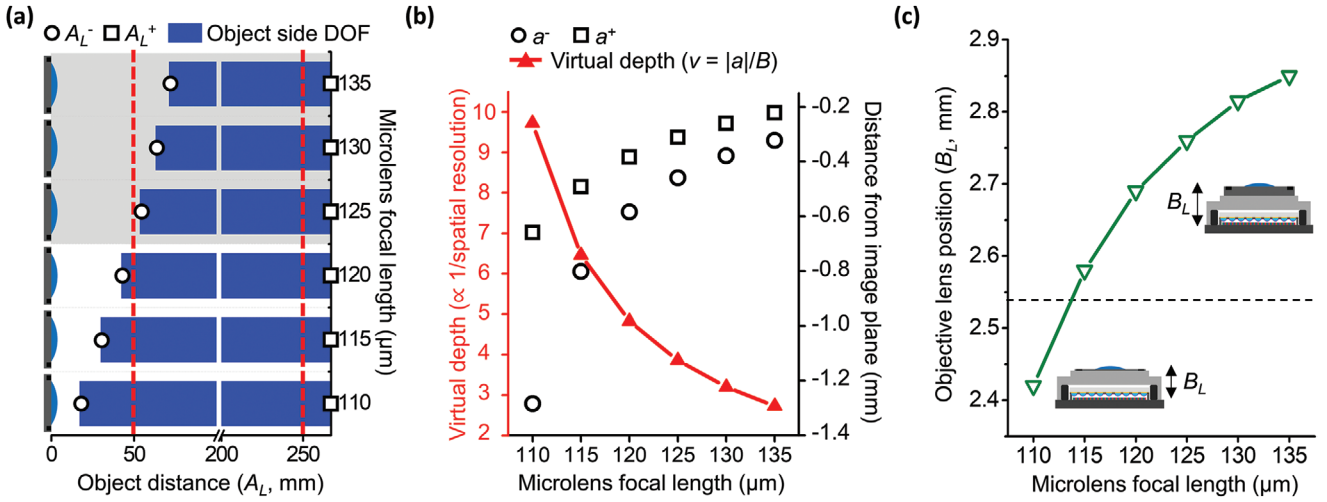

Figure 4. Calculation of microlens focal length and an objective lens position for packaging ULFC with the minimum total track length. a) Image-side DOF and its corresponding DOF range, that is, A_L^- and A_L^+, are determined by using the thin lens equation for an objective lens position (B_L) and f_{OBJ} at each microlens with different f_{MLA}. The tolerable f_{MLA} ranges in 120 μm or less to satisfy a target distance of 50–250 mm, marked as two red dotted lines. b) The object-side DOF range of MLA (from a^- to a^+) and virtual depth (v) are calculated according to each f_{MLA} at given D_{MLA} and B. v is inversely proportional to spatial resolution and thus f_{MLA} is set to 120 μm, which has the minimum value of v. c) An objective lens position (B_L) for the minimum total track length at f_{MLA} is 2.69 mm far from a single image sensor and the final physical dimension of ULFC is 8.4 mm × 8.4 mm × 5.1 mm.

to 120 μm that has the minimum v for the tolerable f_{MLA} range (Figure 4b). An objective lens position (B_L) for the minimum total track length at f_{MLA} is 2.69 mm far from the image sensor (Figure 4c). Total track lengths for both imaging schemes were numerically calculated by using optical ray-tracing simulation (ZEMAX). The calculated objective lens to image sensor distance (B_L) was 2.7 mm for Galilean imaging scheme, while the distance for Keplerian imaging scheme was 4.1 mm under the same conditions of f_{MLA}, f_{OBJ}, and D_{MLA} (Figure S7, Supporting Information). The position of an objective lens is precisely controlled after the vertical camera integration. The ULFC shows the final physical dimension of 8.4 mm × 8.4 mm × 5.1 mm in width, depth, and height, comparable to Raspberry Pi camera V2 (Table S1 and Figure S8, Supporting Information). Note that the Raspberry Pi camera V2 has the B_L of 3.04 mm.

The captured raw microimages were calibrated for high contrast light-field imaging by using the Light-field Imaging Toolkit[31] and finally reconstructed for a disparity map by using an open disparity calculation toolbox based on cost volume filtering[32] The light-field data consist of 5D matrices (43 × 43 × 116 × 85 × 3), including spatial and directional 4D data and RGB color indices. The photograph of fully integrated ULFC is as shown in **Figure 5**a. In experiment, high contrast raw microimages were obtained from numeric cube targets located at 5, 10, and 25 cm, respectively (Figure 5b). The magnified microimages clearly indicate that the Galilean imaging scheme results in upright and repeated microimages. The horizontal parallax images were obtained by collecting and rearranging all the pixels on the left and the right edges of each microimage, depending on the position of dedicated microlens (Figure 5c). The depth refocusing was performed on the different position targets by shifting and summing the pixels of sub-aperture images (Figure 5d). The left image focuses on the front target (5 cm) and the right image focuses on the rear target (25 cm) including background. Each focus is marked with an asterisk "*" (More light-field renderings and other imaging performances such as field-of-view and optical aberrations in Figures S9 and S10, Supporting Information). The depth map was finally estimated from the calibrated 5D light-field data, based on the sum of absolute differences and the sum of gradient differences (Figure 5e). For comparison, the sub-aperture images and depth estimation of the numeric cube targets are also obtained by using LFC without MIM-OA microapertures (Figure 5f,g). As a result, the ULFC substantially improves both the image contrast and the image resolution, resulting in high accuracy for the depth map estimation. Torso plasters and finger posture were further captured for high-resolution 3D depth maps estimation (Figure 5h,i). The plasters are 7.5 and 25 cm far from the ULFC and the index finger, middle finger, and thumb are at 5, 13, and 20 cm positions, respectively. The 3D depth maps clearly distinguish the plaster's eye, nose, and mouth as well as recognize the finger posture.

In summary, we have successfully demonstrated the ultrathin LFC for high contrast and high-resolution light-field imaging using inverted MLA with a MIM-OA. The ULFC involves the microfabrication of MIM-iMLA and the camera packaging of an objective lens, MIM-MLA, and a single image sensor. The thin metal-insulator-thick metal layer fully absorbs the optical crosstalk between neighboring microlenses in the whole visible region. The physical dimension of ULFC shows 8.4 mm × 8.4 mm × 5.1 mm. The light-field rendering clearly demonstrates that the ULFC not only achieves high contrast light-field imaging but also improves the accuracy of 3D depth map estimation. This ultrathin and high contrast LFC can provide a new platform for low cost and compact 3D cameras in healthcare, biometric, automated inspection, or mobile camera applications.

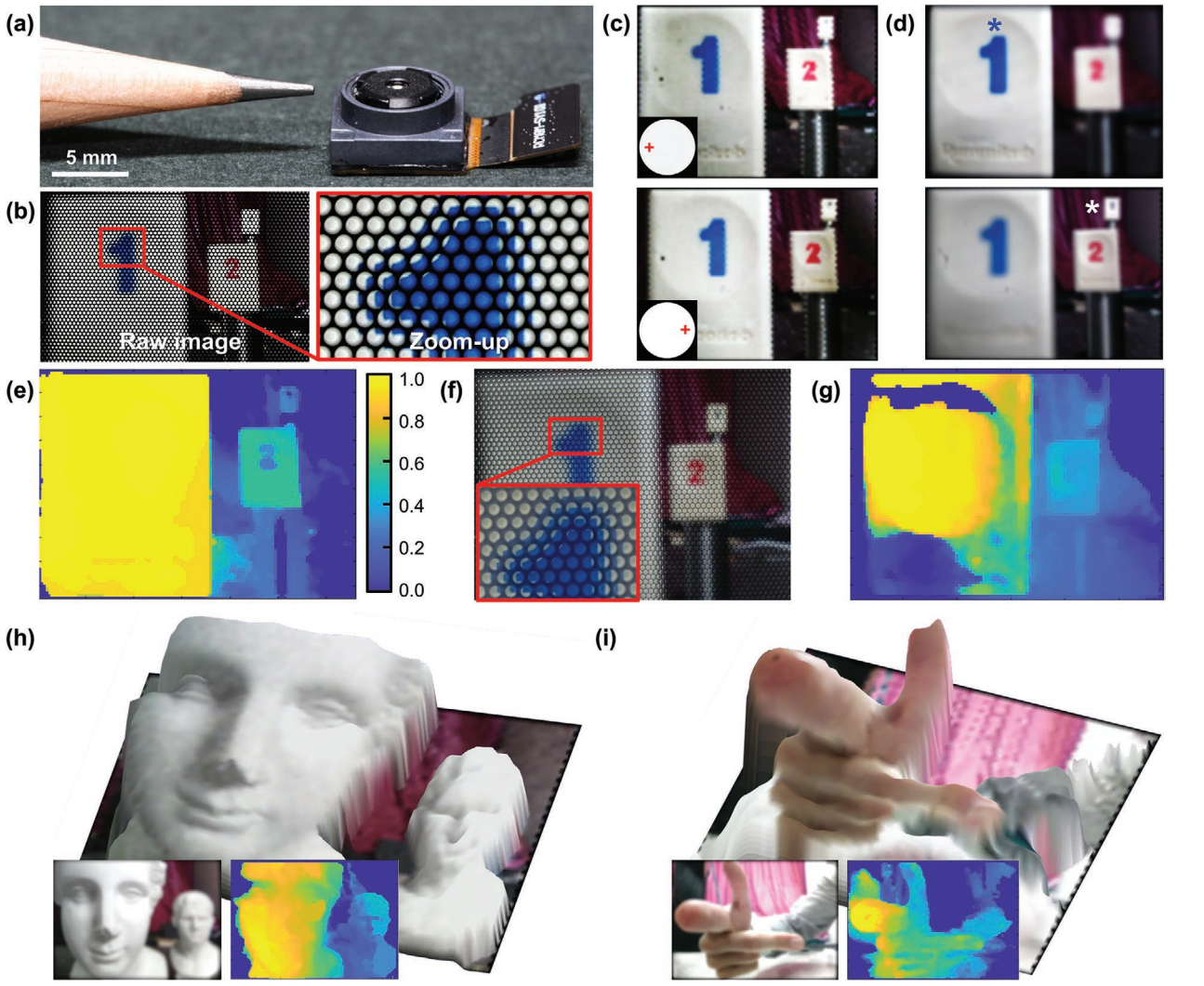

Figure 5. High contrast light-field imaging. a) Photograph of ULFC comprising an objective lens, MIM-iMLA, and CMOS image sensor. b) Raw microimage from ULFC and zoom-up image of three different located numeric cube targets at 5 cm (number 1), 10 cm (number 2), and 25 cm (number 3), respectively. c) Rendered perspective images of ULFC at different view points. d) Digitally refocused images at 5 cm (left) and 25 cm (right) in distance. e) Depth map estimation of cubes at different positions. f) Raw microimage from LFC without MIM-OA and zoom-up image of the same objects. g) Depth map estimation from (f). h) 3D depth estimation of two plaster torso statues at 7.5 and 25 cm away from the ULFC. i) 3D depth estimation of finger poses at 5, 13, and 20 cm of finger positions.

Experimental Section

Experimental Setup and Performance Evaluation: Two different microimage acquisition experiments were conducted to evaluate the performance of MIM-iMLA. Each microimage from MLA and MIM-iMLA was first obtained without an objective lens to compare the image contrast of individual microimages. Each microlens camera was mounted on a Raspberry Pi camera module and precisely aligned along an optical rail. An LED display panel was fixed on the rail at 10 cm far from the camera to capture the microimages. Each microimage was transferred to Image J software to analyze the intensity profiles. Second, raw microimages from both LFC without MIM-OA and ULFC were acquired and reconstructed to light-field image in order to measure the resolving power using the same experimental setup. The Quick MTF software measures the quantitative MTF curves based on a slanted-edge method after the raw light-field rendering.

5D Light-Field Data Calibration and Depth Map Estimation Process: Raw microimages consist of 2464 × 3280 × 3 color matrices. The raw images were reconstructed into 5D radiance arrays during the data calibration procedure according to the directional (u, v) and spatial (s, t) information, including RGB channels (c). Using the calibration data that displays the center points of the microimage, indices (u, v) represent the position of each microlens and indices (s, t) represents the pixel within the microimage, respectively. The raw microimages were separated into R, G, and B channels, and then reconstructed into a 4D radiance array of $L(u, v, s, t)$ for each channel microimage using the Light-field imaging toolkit.[31] The 4D arrays with different color channels were combined to form 5D radiance arrays of $L(u, v, s, t, c)$. Light-field images from the 5D arrays contain optical aberrations caused by the objective lens and the MLA as shown in Figure S10, Supporting Information. These aberrations were estimated from spatially variant epipolar plane image slope and fully corrected by solving an energy minimization problem under a constant depth assumption.[32] The depth estimation algorithm was based on the phase shift in 2D Fourier domain for stereo matching between sub-aperture images with very narrow baseline.[32] The disparity map was calculated by measuring the cost volume and by matching the

similarity between the center and the sub-aperture images for estimating the stereo correspondences. This method calculates the disparity difference between pixels by using two complementary costs to match sub-aperture images, that is, the sum of absolute difference and the sum of gradient difference, which exhibits pixel-level accuracy. The calculated disparity map was sequentially refined by using multi-label optimization, iterative refinement process, and weighted median filtering of the cost slices. The final depth map was estimated by using the light-field parameters such as angular resolution of ULFC, the lens pitch, diameter, and a single-pixel size. All the processes were implemented in MATLAB.

Supporting Information

Supporting Information is available from the Wiley Online Library or from the author.

Acknowledgements

This work was supported by the National Research Foundation of Korea, funded by the Ministry of Science and ICT (2016R1A2B3013061115), the Technology Innovation Program funded by the Ministry of Trade, Industry and Energy (20012464), and funded by Ministry of Health & Welfare (HI16C1111010020), Republic of Korea.

Conflict of Interest

The authors declare no conflict of interest.

Keywords

depth estimation, high resolution, light-field camera, metal–insulator–metal absorber, microlens arrays

Received: September 24, 2020
Revised: December 8, 2020
Published online:

[1] C. Schmalz, F. Forster, A. Schick, E. Angelopoulou, *Med. Image Anal.* **2012**, *16*, 1063.
[2] J. Kittler, A. Hilton, M. Hamouz, J. Illingworth, in *2005 IEEE Computer Society Conf. on Computer Vision and Pattern Recognition (CVPR'05)–Workshops*, IEEE, Piscataway, NJ **2005**, p. 114, https://doi.org/10.1109/CVPR.2005.377.
[3] S. Tijmons, G. C. de Croon, B. D. Remes, C. De Wagter, M. Mulder, *IEEE Trans. Robotics* **2017**, *33*, 858.
[4] A. Markman, J. Wang, B. Javidi, *Optica* **2014**, *1*, 332.
[5] H. Golnabi, A. Asadpour, *Robotics and Computer-Integrated Manufacturing* **2007**, *23*, 630.
[6] S.-P. Yang, J.-J. Kim, K.-W. Jang, W.-K. Song, K.-H. Jeong, *Opt. Lett.* **2016**, *41*, 1285.
[7] S. P. Yang, J. B. Kim, Y. H. Seo, K. H. Jeong, *Adv. Opt. Mater.* **2020**, 2000395.
[8] J. Geng, *Adv. Opt. Photonics* **2011**, *3*, 128.
[9] F. Chiabrando, R. Chiabrando, D. Piatti, F. Rinaudo, *Sensors* **2009**, *9*, 10080.
[10] R. Ng, M. Levoy, M. Bredif, G. Duval, M. Horowitz, P. Hanrahan, *Stanford Tech Report CTSR* **2005**, *1*, 11.
[11] Z. Cai, X. Liu, X. Peng, Y. Yin, A. Li, J. Wu, B. Z. Gao, *Opt. Express* **2016**, *24*, 20324.
[12] M. Martínez-Corral, B. Javidi, *Adv. Opt. Photonics* **2018**, *10*, 512.
[13] C. Perwass, L. Wietzke, in *Human Vision and Electronic Imaging XVII*, *Proc. SPIE*, Vol. *8291*, SPIE, Bellingham, WA **2012**, p. 829108.
[14] N. K. Kalantari, T.-C. Wang, R. Ramamoorthi, *ACM Trans. Graphics* **2016**, *35*, 1.
[15] Y. Yoon, H.-G. Jeon, D. Yoo, J.-Y. Lee, I. S. Kweon, in *Proceedings of the IEEE Int. Conf. on Computer Vision Workshops (ICCVW)*, IEEE, Piscataway, NJ **2015**, pp. 57–65.
[16] R. J. Lin, V.-C. Su, S. Wang, M. K. Chen, T. L. Chung, Y. H. Chen, H. Y. Kuo, J.-W. Chen, J. Chen, Y.-T. Huang, *Nat. Nanotechnol.* **2019**, *14*, 227.
[17] M.-K. Chen, C. H. Chu, R. J. Lin, J.-W. Chen, Y.-T. Huang, T.-T. Huang, H. Y. Kuo, D. P. Tsai, *Jpn. J. Appl. Phys.* **2019**, *58*, SK0801.
[18] Z.-B. Fan, H.-Y. Qiu, H.-L. Zhang, X.-N. Pang, L.-D. Zhou, L. Liu, H. Ren, Q.-H. Wang, J.-W. Dong, *Light: Sci. Appl.* **2019**, *8*, 1.
[19] P.-Y. Hsieh, P.-Y. Chou, H.-A. Lin, C.-Y. Chu, C.-T. Huang, C.-H. Chen, Z. Qin, M. M. Corral, B. Javidi, Y.-P. Huang, *Opt. Express* **2018**, *26*, 10981.
[20] S.-I. Bae, K. Kim, S. Yang, K.-w. Jang, K.-H. Jeong, *Opt. Express* **2020**, *28*, 9082.
[21] A. Lumsdaine, T. Georgiev, in *2009 IEEE Int. Conf. on Computational Photography (ICCP)*, IEEE, Piscataway, NJ **2009**.
[22] D. Keum, K.-W. Jang, D. S. Jeon, C. S. Hwang, E. K. Buschbeck, M. H. Kim, K.-H. Jeong, *Light: Sci. Appl.* **2018**, *7*, 1.
[23] A. Brückner, J. Duparré, R. Leitel, P. Dannberg, A. Bräuer, A. Tünnermann, *Opt. Express* **2010**, *18*, 24379.
[24] Y. M. Song, Y. Xie, V. Malyarchuk, J. Xiao, I. Jung, K.-J. Choi, Z. Liu, H. Park, C. Lu, R.-H. Kim, R. Li, K. B. Crozier, Y. Huang, J. A. Rogers, *Nature* **2013**, *497*, 95.
[25] K. Kim, K.-W. Jang, J.-K. Ryu, K.-H. Jeong, *Light: Sci. Appl.* **2020**, *9*, 28.
[26] H. Song, L. Guo, Z. Liu, K. Liu, X. Zeng, D. Ji, N. Zhang, H. Hu, S. Jiang, Q. Gan, *Adv. Mater.* **2014**, *26*, 2737.
[27] Z. Li, E. Palacios, S. Butun, H. Kocer, K. Aydin, *Sci. Rep.* **2015**, *5*, 1.
[28] K. Aydin, V. E. Ferry, R. M. Briggs, H. A. Atwater, *Nat. Commun.* **2011**, *2*, 1.
[29] J.-B. You, W.-J. Lee, D. Won, K. Yu, *Opt. Express* **2014**, *22*, 8339.
[30] U. Park, H.-C. Choi, A. K. Jain, S.-W. Lee, *IEEE Trans. Information Forensics Security* **2013**, *8*, 1665.
[31] J. Bolan, E. Hall, C. Clifford, B. Thurow, *SoftwareX* **2016**, *5*, 101.
[32] H.-G. Jeon, J. Park, G. Choe, J. Park, Y. Bok, Y.-W. Tai, I. So Kweon, in *Proceedings of the IEEE Conf. on Computer Vision and Pattern Recognition (CVPR)*, IEEE, Piscataway, NJ **2015**, pp. 1547–1555.